HOKKAIDO UNIVERSITY

Title	High-energy x-ray nanotomography introducing an apodization Fresnel zone plate objective lens
Author(s)	Takeuchi, Akihisa; Uesugi, Kentaro; Uesugi, Masayuki; Toda, Hiroyuki; Hirayama, Kyosuke; Shimizu, Kazuyuki; Matsuo, Koichi; Nakamura, Takashi
Citation	Review of Scientific Instruments, 92(2), 023701 https://doi.org/10.1063/5.0020293
Issue Date	2021-02-01
Doc URL	http://hdl.handle.net/2115/83977
Rights	This article may be downloaded for personal use only. Any other use requires prior permission of the author and AIP Publishing. This article appeared in Akihisa Takeuchi, Kentaro Uesugi, Masayuki Uesugi, Hiroyuki Toda, Kyosuke Hirayama, Kazuyuki Shimizu, Koichi Matsuo, and Takashi Nakamura , "High-energy x-ray nanotomography introducing an apodization Fresnel zone plate objective lens", Review of Scientific Instruments 92, 023701 (2021) and may be found at https://doi.org/10.1063/5.0020293.
Type	article
File Information	5.0020293.pdf

High-energy x-ray nanotomography introducing an apodization Fresnel zone plate objective lens

Akihisa Takeuchi, Kentaro Uesugi, Masayuki Uesugi, Hiroyuki Toda, Kyosuke Hirayama, Kazuyuki Shimizu, Koichi Matsuo, and Takashi Nakamura

View Online   Export Citation   CrossMark

ARTICLES YOU MAY BE INTERESTED IN

High-energy x-ray nanotomography introducing an apodization Fresnel zone plate objective lens

View Online   Export Citation   CrossMark

Akihisa Takeuchi,[1,a] (iD) Kentaro Uesugi,[1] (iD) Masayuki Uesugi,[1] (iD) Hiroyuki Toda,[2] (iD) Kyosuke Hirayama,[2]
Kazuyuki Shimizu,[2,3] (iD) Koichi Matsuo,[4] (iD) and Takashi Nakamura[5] (iD)

AFFILIATIONS

[1] Japan Synchrotron Radiation Research Institute, SPring-8, 1-1-1, Kouto, Sayo, Hyogo 679-5198, Japan
[2] Department of Mechanical Engineering, Kyushu University, 744, Motooka, Nishi Ward, Fukuoka City, Fukuoka 819-0395, Japan
[3] Department of Materials Science and Engineering, Iwate University, 4-3-5 Ueda, Morioka City, Iwate 020-8551, Japan
[4] Laboratory of Cell and Tissue Biology, Keio University School of Medicine, 35 Shinanomachi, Shinjuku-ku, Tokyo 160-8582, Japan
[5] Division of Mechanical and Aerospace Engineering, Faculty of Engineering, Hokkaido University, Kita 13, Nishi 8, Kita-ku,
 Sapporo, Hokkaido 060-8628, Japan

[a] Author to whom correspondence should be addressed: take@spring8.or.jp

ABSTRACT

In this study, high-energy x-ray nanotomography (nano-computed tomography, nano-CT) based on full-field x-ray microscopy was developed. Fine two-dimensional and three-dimensional (3D) structures with linewidths of 75 nm–100 nm were successfully resolved in the x-ray energy range of 15 keV–37.7 keV. The effective field of view was ~60 μm, and the typical measurement time for one tomographic scan was 30 min–60 min. The optical system was established at the 250-m-long beamline 20XU of SPring-8 to realize greater than 100× magnification images. An apodization Fresnel zone plate (A-FZP), specifically developed for high-energy x-ray imaging, was used as the objective lens. The design of the A-FZP for high-energy imaging is discussed, and its diffraction efficiency distribution is evaluated. The spatial resolutions of this system at energies of 15 keV, 20 keV, 30 keV, and 37.7 keV were examined using a test object, and the measured values are shown to be in good agreement with theoretical values. High-energy x-ray nano-CT in combination with x-ray micro-CT is applied for 3D multiscale imaging. The entire bodies of bulky samples, ~1 mm in diameter, were measured with the micro-CT, and the nano-CT was used for nondestructive observation of regions of interest. Examples of multiscale CT measurements involving carbon steel, mouse bones, and a meteorite are discussed.

Published under license by AIP Publishing. https://doi.org/10.1063/5.0020293

I. INTRODUCTION

High-spatial-resolution x-ray computed tomography (CT) based on a full-field x-ray microscope, known as x-ray nanotomography (nano-computed tomography, nano-CT), is widely used for realizing nanometer-scale three-dimensional (3D) nondestructive observation of the inner structures of objects. Most variants, including those based on synchrotron-radiation (SR) sources and laboratory sources, are designed to be used at an x-ray energy range of less than 15 keV,[1–13] which is sufficient for many types of materials with sample dimensions less than several tens of micrometers [the typical field of view (FOV) for nano-CT systems]. However, for 3D imaging of high-Z materials, x rays must possess

higher energy (several tens of keV). For various types of materials, including metals, minerals, and ceramics, the high penetrating power of high-energy x rays relaxes the requirements for the sample size to the millimeter order and enables multiscale CT imaging through the use of nano-CT and micro-CT to obtain wide FOVs. Because no subdivision of the bulky sample is required, *in situ*, *ex situ*, and operando measurements are easily achieved. In some domains, such as electrical devices and batteries, it is important to be able to observe the internal structures at the nanometer scale while maintaining the bulk state of the sample. However, the high penetrating power of high-energy x rays causes low sensitivity because of its low interaction with matter. This problem can be solved by employing phase-contrast imaging, which can

improve sensitivity by one to three orders of magnitude compared to conventional absorption contrast.[14] Low radiation damage, another advantage of high-energy x rays, enables high-resolution observations of biological specimens and soft materials. Thus, the demand for high-energy x-ray nano-CT is significant in many domains. Nevertheless, only a few nano-CT systems support this high-energy x-ray application. Only nano-holotomography at the European Synchrotron Radiation Facility, which uses Kirkpatrick–Baez (KB) mirrors, has been practically used in the x-ray region over 30 keV.[15–17] Nano-CT, which uses compound refractive lenses (CRLs) for energies up to 50 keV, is equipped at the P05 imaging beamline of PETRA III,[18–20] although any results involving high-energy x-ray nano-CT are yet to be reported. Even if the conditions are lowered to 20 keV, only the nano-CT that uses a Fresnel zone plate (FZP) at the Swiss Light Source can be considered a high-energy-compatible system.[21]

There are two main challenges in realizing high-energy x-ray nano-CT. The first is the difficulty in fabricating optical devices with sufficient precision and efficiency. Second, a particularly long optical tube is required to achieve high magnification, as the focal length of an optical device increases as the x-ray energy requirements increase.

We developed a high-energy x-ray Zernike phase-contrast full-field microscope at the SR facility, SPring-8, Japan. Our system enabled 3D nanotomographic imaging in the x-ray energy region of 15 keV–37.7 keV. Both the aforementioned challenges were overcome as follows. To overcome the first challenge, an apodization FZP (A-FZP), which can be used to obtain high efficiency in high-energy x-ray regions, was employed as the objective lens.[22] To address the second challenge, the system was established at the 250-m-long beamline 20XU (BL20XU) of SPring-8,[23] thereby enabling greater than 100× high magnification even for x-ray energy regions of several tens of kilo-electron volt.

In this paper, an A-FZP is first described in terms of its use as an objective lens for high-energy x-ray nano-CT. Next, we describe the development of a full-field high-energy x-ray microscope, after which we present the experimental results of high-energy x-ray 2D and 3D nano-imaging. Finally, some applications are presented.

II. A-FZP FOR HIGH-ENERGY X-RAY OBJECTIVE LENS

In nano-CT measurements, in which the object is rotated and its transmission images are acquired from all angles, its 3D FOV is limited by the smaller lateral FOV and the depth of field (DOF) of the optical system. If the lateral FOV is larger than the DOF, then the optical system can be considered off-axis-aberration-free, and the conventional backprojection method for a parallel-beam projection geometry is applicable for nano-CT reconstruction, regardless of the illumination.[24–26] It has been proven in FZP optics that the lateral FOV determined by every Seidel's off-axis aberration (coma, astigmatism, distortion, and field of curvature) always satisfies this condition in the hard-x-ray region.[27,28] Therefore, FZPs are promising devices as objective lenses for x-ray nano-CT.

However, one problem associated with FZP optics is the trade-off between spatial resolution and efficiency. Furthermore, this
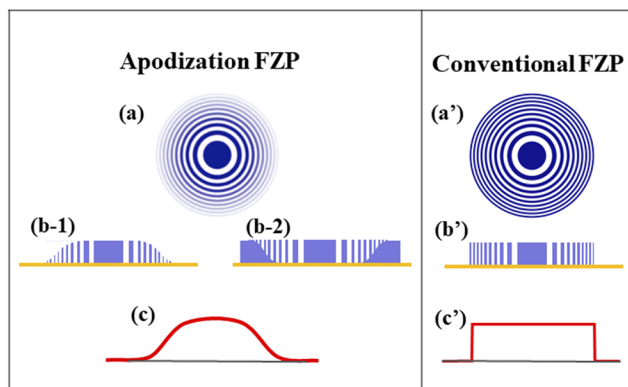

FIG. 1. A-FZP (a) overview, (b) cross section, and (c) efficiency distribution. A conventional FZP is included for comparison [(a')–(c')].

trade-off becomes more severe as the x-ray energy increases. The spatial resolution of an FZP is determined by the outermost zone width d, while its diffraction efficiency is determined by the zone thickness t, which must be high for high-energy x rays. Therefore, a high aspect ratio, t/d, is required to achieve high resolution and high efficiency. Although FZP manufacturing techniques
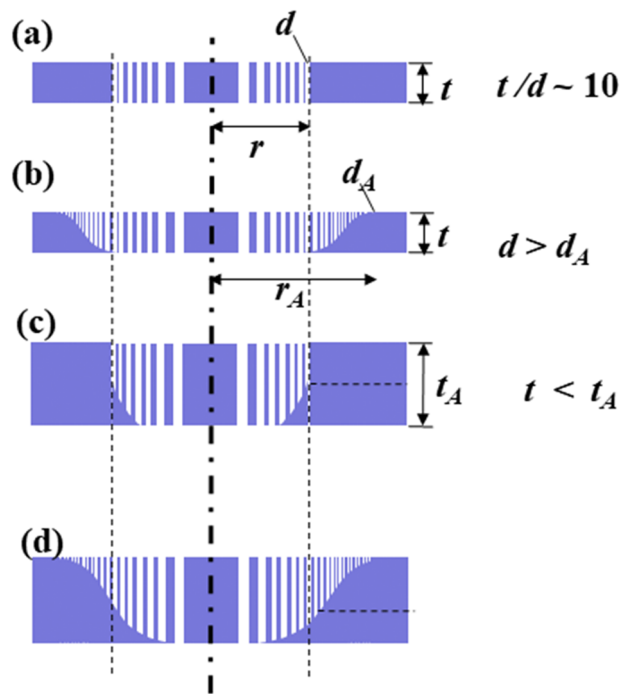

FIG. 2. Comparison of cross-sectional structures between (a) conventional FZP with radius r, thickness t, and outermost zone width d; (b) A-FZP for high resolution with radius r_A ($>r$), thickness t, and outermost zone width d_A ($<d$); (c) A-FZP for high efficiency with radius r, thickness t_A ($>t$), and outermost zone width d; and (d) A-FZP for high resolution and high efficiency with radius r_A, thickness t_A, and outermost zone width d_A.

TABLE I. Typical parameters of the A-FZP used (NTT Advanced Technology, Japan).

Base plate	Si 10 mm × 10 mm × 0.625 mm
Membrane	Ru 20 nm/SiC 2 μm/SiN 0.3 μm
Zone material	Ta
Diameter	310 μm
Outermost zone width	100 nm
Thickness of inner-half zones	2 μm
Zone number	775
Focal length at 30 keV	750 mm

FIG. 3. Measured first-order diffraction efficiency of the A-FZP. Theoretical values of tantalum FZPs with thicknesses of 1 μm, 1.5 μm, and 2 μm are also depicted.

have advanced through state-of-the-art electron beam lithography, it has been technically difficult to realize an aspect ratio higher than 10. Therefore, most FZP optics have been used only in an energy region of ~10 keV or lower. Thus far, various methods and innovations have been proposed to increase the aspect ratio or the interaction zone, for example, stacked FZPs,[29,30] double patterning,[31] zone-doubled FZPs,[32,33] double-sided FZPs,[34] total-reflection FZPs,[35] and vertical directionality-controlled metal-assisted chemical etching.[36] Multilayer FZPs,[37–39] which make it considerably easier to fabricate thick zone patterns compared to lithography FZPs, have been developed and used to realize full-field x-ray microscopy at several tens of kilo-electron volt;[40] however, they have not yet been practically applied.

We used an A-FZP for high-energy x-ray imaging (Fig. 1).[22] Its zone thickness gradually decreased from the central to the outer region [Figs. 1(a) and 1(b)]. Accordingly, the diffraction efficiency gradually decreased from the inner to the outer region [Fig. 1(c)], thereby realizing an apodization filter.[41] An A-FZP structure in which the zone thickness gradually changes is realized by utilizing the micro-loading effect, which decreases the etching depth while simultaneously decreasing the pattern width using dry etching.[42,43]

Another advantage offered by an A-FZP is that the difference in zone thickness between the central and outer regions makes it technically possible to fabricate finer outer zones and/or thicker inner zones than in conventional FZPs (Fig. 2). The former realizes high resolution [Fig. 2(b)], while the latter realizes high efficiency [Fig. 2(c)] and is appropriate for use in high-energy x-ray regions. Notably, high-resolution and high-efficiency A-FZPs can be fabricated [Fig. 2(d)]. However, a significant difference in zone thickness between the central and outer regions decreases the spatial
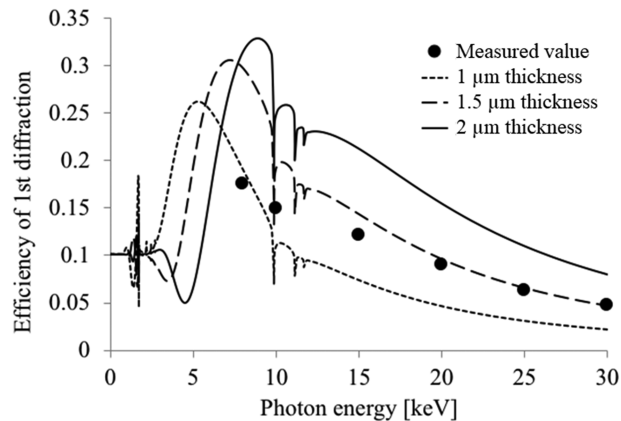
resolution and efficiency. The thickness ratio between the thickest and thinnest zones should be less than 2 to satisfy Rayleigh's quarter-wavelength rule, considering that an optimized FZP is a half-wavelength shifter.

The typical parameters of the A-FZP used in this study are listed in Table I. This device was fabricated via electron-beam lithography and reactive-ion etching at Nippon Telegraph and Telephone (NTT) Advanced Technology.[43,44] The inner-half zones were completely etched (over-etched), whereas the outer-half zones were partially etched to realize a gradually changing zone thickness utilizing the micro-loading effect. Therefore, the thicknesses of the outer-half regions gradually decreased from the interior to the exterior.

Figure 3 depicts the relationship between the x-ray energy and efficiency measured for the first-order diffraction of the A-FZP. In addition, it shows the theoretical efficiencies of conventional FZPs with uniform zone thickness, expressed as

$$\text{Efficiency} = 1/\pi^2 \{1 + \exp(-4\pi\beta t/\lambda) - 2\exp(-2\pi\beta t/\lambda)\cos(-2\pi\delta t/\lambda)\},$$

where λ is the wavelength and $1 - \delta + i\beta$ is the complex refractive index of the zone material.[45,46] A diffraction efficiency of ~10% was achieved at 20 keV. Figure 4 depicts a 2D
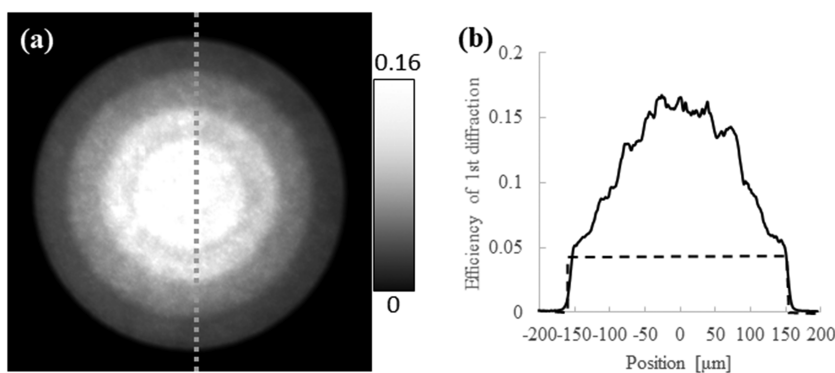
FIG. 4. (a) 2D distribution of first-order diffraction efficiency of the A-FZP and (b) its cross-sectional profile. Theoretical values of a conventional FZP with 1 μm thickness are also shown by the broken line.

distribution and the cross-sectional profile of the A-FZP for the first-order diffraction efficiency. The measurement method is described in the literature.[22] The efficiency gradually changes from the inner to outer region, confirming the realization of apodized apertures. The theoretical values of the diffraction efficiency distribution of a conventional FZP, which is assumed to have the same outermost zone width as the A-FZP and uniform zone thickness technically limited by the aspect ratio, are also shown in Fig. 4(b). The conventional FZP has a uniform distribution of the diffraction efficiency, whereas the A-FZP has notably higher diffraction efficiencies in the inner regions. This results in the A-FZP having a higher overall diffraction efficiency than the conventional FZP.

III. FULL-FIELD HIGH-ENERGY X-RAY MICROSCOPY

A. Overview of the system

Figure 5(a) depicts the high-energy x-ray nano-CT system based on full-field x-ray microscopy at BL20XU. Radiation produced using a 173-pole planar undulator, which was installed in the SPring-8 8 GeV electron storage ring, was monochromatized by passing it through a liquid-nitrogen-cooled Si (111) double-crystal monochromator. The high harmonics were suppressed by detuning the monochromator. Hollow-cone illumination was produced using a rotating sector condenser zone plate (CZP), comprised of eight concentrically arranged linear diffraction gratings with a half-pitch of 200 nm.[47,48] A tantalum center beam stop (diameter: 250 μm and thickness: 1000 μm) and tantalum four-jaw slit with an opening size of 70 μm × 70 μm were used for diffraction order sorting. This illuminating system provided a photon flux density of 20-keV, delivering ~1.0 × 10^{14} photons/s/mm^2 at the sample location. The sample was mounted on a high-precision, slide-guide rotation stage for tomographic scanning (CRA070-002, Kohzu Precision Co. Ltd., Japan). The wobble of the rotation stage was estimated to be less than 100 nm.[10] The A-FZP was used as the objective lens. Zernike phase plates (ZPPs, NTT Advanced Technology, Japan) optimized for imaging at x-ray energies of 20 keV, 30 keV, and 37.7 keV were installed on the back focal plane of the objective lens. The illuminating system, sample stage, objective A-FZP, and ZPP were installed in the first experimental hutch, located in the SPring-8 Storage Ring Building. A beam stop and x-ray image detector were installed in the second experimental hutch, located in the Medium-Length Beamline Facility built outside of the Storage Ring Building. The x-ray image detector was composed of a visible-light conversion unit (M11427, Hamamatsu Photonics, Japan) and a scientific complementary metal–oxide–semiconductor (sCMOS) camera (C13440-20CU, Hamamatsu Photonics, Japan). The effective pixel size could
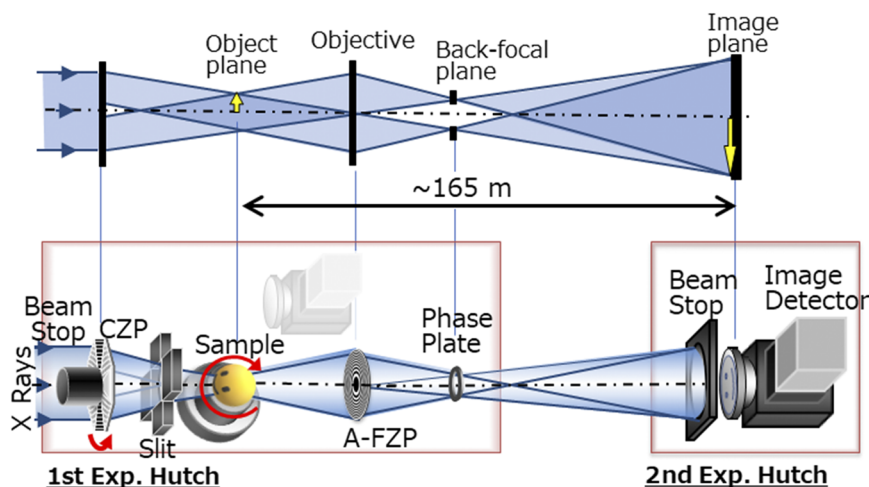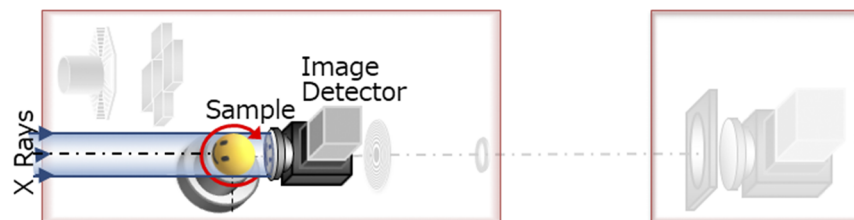

FIG. 5. (a) High-energy x-ray nano-CT and (b) micro-CT.

TABLE II. Parameters of high-energy x-ray nano-CT and micro-CT.

Mode	FOV (μm)	Res. (μm)	Voxel (μm)	Pixel format
Nano-CT	60–80	0.15–0.2	0.03–0.04	2048 × 2048
Micro-CT	1000	~2	0.5	2048 × 2048

be varied from 6.5 μm to 19 μm by using a two-lens-coupled system inside M11427. A single crystal of $Lu_3Al_5O_{12}$:Ce^+ (LuAG:Ce) or $Gd_3Al_2Ga_3O_{12}$:Ce^+ (GAGG:Ce), or a coating of powder-type P43 (Gd_2O_2S:Tb^+) phosphor, was used as a visible-light converter. The tomography scan was performed in the on-the-fly scan mode. The transmission x-ray images of the sample at different rotation angles were typically acquired with a 0.1° interval in each tomography scan. The convolution backprojection method was used for tomographic reconstruction. The typical parameters of the nano-CT are listed in Table II.

B. Design of high-magnification optical system for high-energy x-ray region

The positions of the sample at the object plane, the objective lens, and the image detector at the image plane are strictly determined by using the Gaussian lens formula,

$$f = 1/z_1 + 1/z_2, \qquad (1)$$

where f, z_1, and z_2 denote the focal length of the objective lens, the sample-to-objective distance, and the objective-to-detector distance, respectively. Furthermore, z_1 and z_2 can be expressed as $L = z_1 + z_2$ and $M = z_2/z_1$, where L and M are the optical tube length of the full-field microscope and the magnification of the optical system, respectively. Therefore, the relationship between L and M is derived using the Gaussian lens formula,

$$L = \frac{(M+1)^2}{M} f. \qquad (2)$$

For large values of M, L can be approximated as

$$L \sim Mf. \qquad (3)$$

The focal distance of the FZP is approximately given from the Fresnel diffraction formula,

$$r_n{}^2 = n\lambda f, \qquad (4)$$

where r_n denotes the radius of the nth zone and λ is the x-ray wavelength.[27] Using these equations, we can derive the following relationship between the optical tube length and the x-ray wavelength:

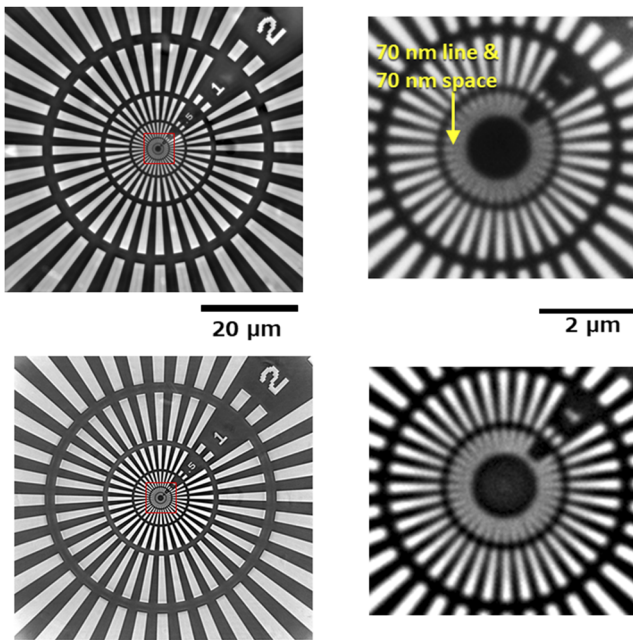$$L \propto \frac{M}{\lambda} (\propto ME), \qquad (5)$$

FIG. 6. Zernike-phase-contrast (above) and absorption-contrast (below) x-ray images of the tantalum test chart (XRESO-50HC, NTT Advanced Technology, Japan) and their magnified central regions (right). The x-ray energy was 15 keV. The magnification was 440×. A 200-μm-thick LuAG:Ce single-crystal plate (Hamamatsu Photonics, Japan) was used as the scintillator for the x-ray image detector. The effective pixel size was 31.4 nm, and the exposure time was 10 s.

FIG. 7. Zernike-phase-contrast (above) and absorption-contrast (below) x-ray images of the tantalum test chart and their magnified central regions (right). The x-ray energy was 20 keV. The magnification was 330×. A 200-μm-thick LuAG:Ce single-crystal plate (Hamamatsu Photonics, Japan) was used as the scintillator for the x-ray image detector. The effective pixel size was 31.4 nm, and the exposure time was 10 s.
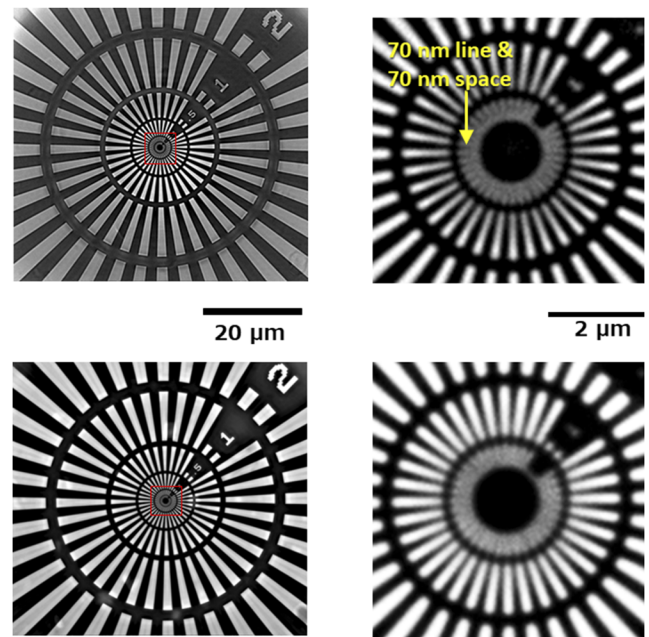
where E denotes the x-ray energy. Therefore, to realize a high-energy x-ray full-field microscope without compromising magnification, one must accordingly increase the optical tube length. In addition, it becomes difficult for image detectors to achieve both high spatial resolution and high efficiency as the x-ray energy increases because a thicker scintillator is required. Therefore, further higher magnification is required so that the x-ray microscope optics can compensate for the resolution degradation of the detector. However, the optical tube length of a typical SR-based full-field x-ray microscope ranges from approximately several meters to several tens of meters and is limited by the size of the experimental hutch, even for an energy of ~10 keV. Therefore, it cannot be further increased for x rays with higher energy. In this study, a significantly large optical tube length was realized by installing the system in the 250-m-long BL20XU undulator beamline of SPring-8.[23] The distance between the first and second experimental hutches is ~165 m, which enables sufficiently high magnification for the high-energy x-ray region. A preliminary experiment with a magnification of 100× for an energy of 82 keV was performed using a multilayer FZP.[40]

IV. EXPERIMENTS

A. Spatial-resolution evaluation for 2D imaging

The performance test for 2D imaging was conducted using a tantalum test chart (XRESO-50HC, NTT Advanced Technology,

Japan) with a fine structure of up to 50-nm lines and 50-nm spaces with 500-nm thickness. The absorption-contrast and Zernike-phase-contrast 2D images for x-ray energies of 15 keV, 20 keV, 30 keV, and 37.7 keV are depicted in Figs. 6–9, respectively. Pattern linewidths as fine as ~70 nm (140 nm full pitch) were resolved at 15 keV and 20 keV (see Figs. 6 and 7). In the case of a full-field microscope using the CZP and FZP, the spatial resolution limit Δ_S for the periodic structure of an object placed at the center of the image circle is

$$\Delta_s = \frac{\lambda}{NA_{CZP} + NA_{FZP}}, \tag{6}$$

where NA_{CZP} and NA_{FZP} represent the numerical aperture of the CZP and FZP, respectively. Equation (6) can be rewritten as

$$\frac{1}{\Delta_s} = \frac{1}{2d_{CZP}} + \frac{1}{2d_{FZP}}, \tag{6'}$$

where d_{CZP} and d_{FZP} represent the half-pattern pitch of the CZP and outermost zone width of the FZP objective lens, respectively, and the relationship between these zone widths and numerical apertures [$d_{CZP} \sim \lambda/(2NA_{CZP})$, $d_{FZP} \sim \lambda/(2NA_{FZP})$] is used.[10,28,48] In the present case ($d_{CZP} = 200$ nm and $d_{FZP} = 100$ nm), using Eq. (6'), the spatial resolution can be rewritten as $\Delta s = 4/3d_{FZP} = 133.3$ nm. The measured value of 140 nm is in good agreement with the theoretical
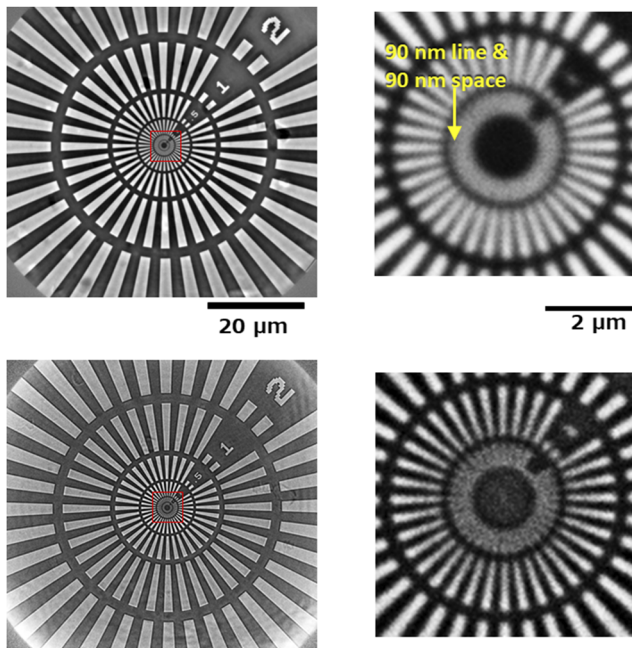

FIG. 8. Zernike-phase-contrast (above) and absorption-contrast (below) x-ray images of the tantalum test chart and their magnified central regions (right). The x-ray energy was 30 keV. The magnification was 210×. A 200-μm-thick GAGG:Ce single crystal plate (Hamamatsu Photonics, Japan) was used as the scintillator for the x-ray image detector. The effective pixel size was 30.9 nm, and the exposure time was 30 s.
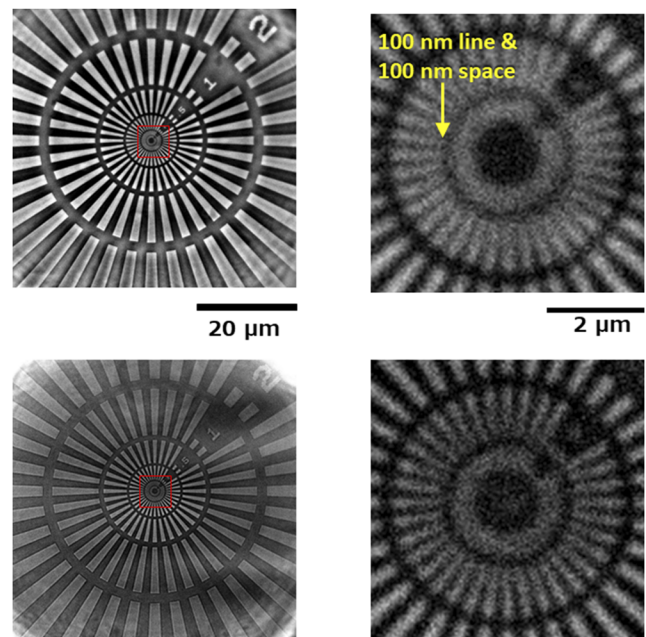

FIG. 9. Zernike-phase-contrast (above) and absorption-contrast (below) x-ray images of the tantalum test chart and their magnified central regions (right). The x-ray energy was 37.7 keV. The magnification was 175×. A 200-μm-thick GAGG:Ce single-crystal plate (Hamamatsu Photonics, Japan) was used as the scintillator for the x-ray image detector. The effective pixel size was 38.9 nm, and the exposure time was 20 s.

TABLE III. Parameters of the artificial, concentric Al/Cu multilayer pattern used as a test object for 3D CT measurements.

Layer	Linewidth
Base	Al 25 μm diameter
1st–4th	Cu/Al 250 nm
5th–8th	Cu/Al 200 nm
9th–12th	Cu/Al 150 nm
13th–16th	Cu/Al 100 nm
17th–20th	Cu/Al 75 nm
21st–24th	Cu/Al 50 nm
25th	Cu 1 μm

value of 133.3 nm. Although the x-ray images obtained at 30 keV and 37.7 keV contain some uneven background noise due to the leakage of other diffraction orders from the A-FZP, linewidths of up to 100 nm (200 nm full pitch) were resolved (see Figs. 8 and 9). For each energy value, the image of the test chart is visible over an FOV greater than 60 μm.

B. Spatial-resolution evaluation for 3D CT imaging

To precisely measure the spatial resolution of 3D tomographic images, an artificial, concentric pattern Al/Cu multilayer material was used as a test sample. Al/Cu was deposited onto a rotating Al wire substrate (diameter: 25 μm) via direct-current magnetron sputtering.[49] The parameters of the concentric pattern are listed in Table III. Figures 10 and 11 present the CT images at x-ray energies of 20 keV and 30 keV, respectively. Figures 10(f) and 11(e) depict the profiles of the lines in Figs. 10(a) and 11(a), respectively. In both images, multilayered Al/Cu patterns as fine as 75 nm in linewidth (150 nm full pitch) are visible, indicating good agreement with the theoretical spatial-resolution value of 133.3 nm described in Sec. IV A.

V. APPLICATIONS OF MULTISCALE 3D X-RAY IMAGING

One of the advantages of using high-energy x rays is their high penetrating power into materials, thereby enabling observations of thick or high-density objects. Accordingly, a multiscale CT was developed at BL20XU by combining a micro-CT, based
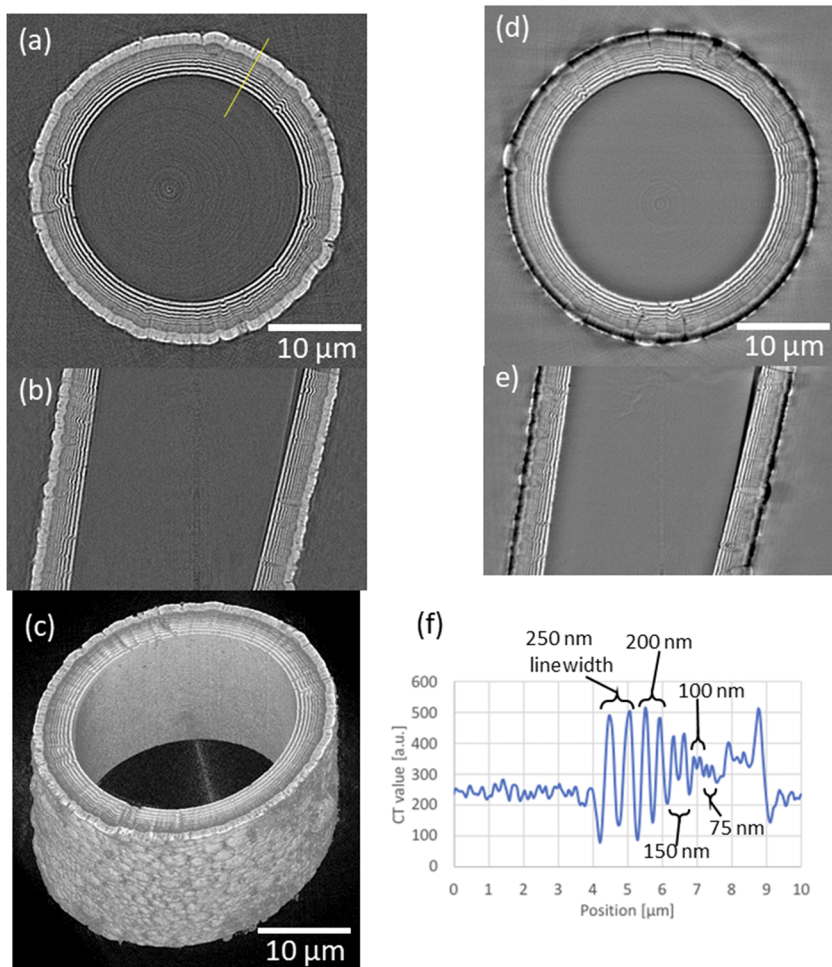

FIG. 10. X-ray nano-CT images of a concentric-pattern Al/Cu multilayer sample with absorption contrast [(a)–(c)] and with Zernike-phase contrast [(d) and (e)]. (f) Profile of the line in (a). The x-ray energy was 20 keV, and the magnification was 330×. A 10-μm-thick P43 powder coating (Hamamatsu Photonics, Japan) was used as the scintillator for the x-ray image detector. The effective pixel size was 43.1 nm, the exposure time was 2 s, and 1800 images were acquired over a 180° rotation.
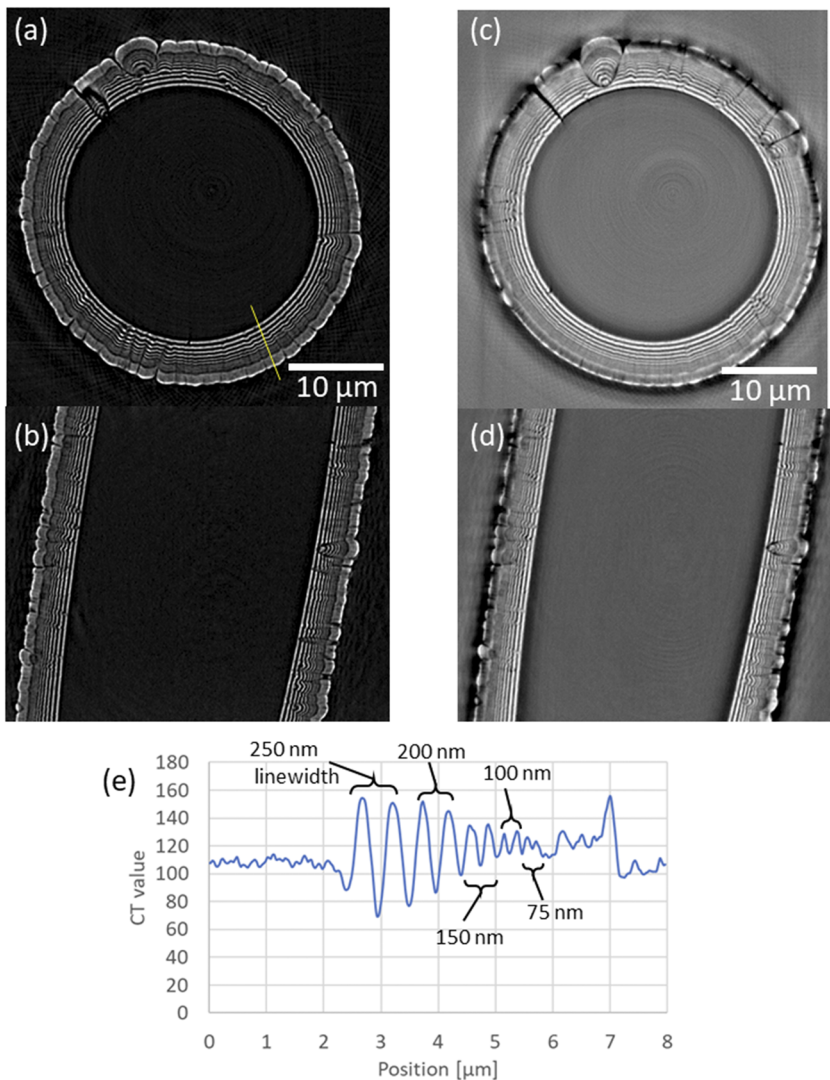
FIG. 11. X-ray nano-CT images of a concentric Al/Cu multilayer pattern with absorption contrast [(a) and (b)] and Zernike-phase contrast [(c) and (d)]. (e) Profile of the line in (a). The x-ray energy was 30 keV. The magnification was 220×. A 200-μm-thick GAGG:Ce single crystal (Hamamatsu Photonics, Japan) was used as the scintillator for the x-ray image detector. The effective pixel size was 30.9 nm, the exposure time was 1 s, and 1800 images were acquired over a 180° rotation.

on simple projection optics [see Fig. 5(b)], and a high-energy x-ray nano-CT.[50] The typical parameters of the micro-CT are listed in Table II. A high-resolution, visible-light conversion-type x-ray camera unit (M11427-51 and C13440-20CU, Hamamatsu Photonics, Japan) was used with 0.5 μm pixel size. A 20-μm-thick GAGG:Ce single crystal was used as the scintillator, which enabled the observation of a diameter of up to 1 mm with a spatial resolution of 1 μm–2 μm. As depicted in Fig. 5, these two measurement modes can be easily switched without dismounting the sample from the holder. Only a few minutes are required for mode switching by sliding the hollow-cone illuminating system and image detector behind the sample in or out. The entire structure of the sample is measured in the micro-CT mode, and the region of interest (ROI) is nondestructively measured in the nano-CT mode. The high penetrating power of x rays used to measure large samples, by contrast, leads to reduced sensitivity. To solve this problem, high-sensitivity

phase-contrast x-ray imaging methods such as Zernike's method (the method selected for this study) or the defocusing method is actively adopted in nano-CT. Here, three applications of multiscale CT are introduced.

A. Dual-phase structure of carbon steel

Figure 12 depicts the virtual cross sections of dual-phase carbon steel, which is an iron–carbon alloy. It includes horizontal, vertical, and oblique cross sections. The alloy composition is Fe–0.1C–5Mn–1Si, comprising a ferrite matrix and metastable retained austenite, which has a volume fraction of ~22%. The densities of the ferrite and austenite phases are 7.71 g/cm^3 and 7.65 g/cm^3, respectively. Although the density difference between both phases in the dual-phase carbon steel is only 0.7%, the metastable retained austenite phase is clearly observed, as shown in Fig. 12. Because of
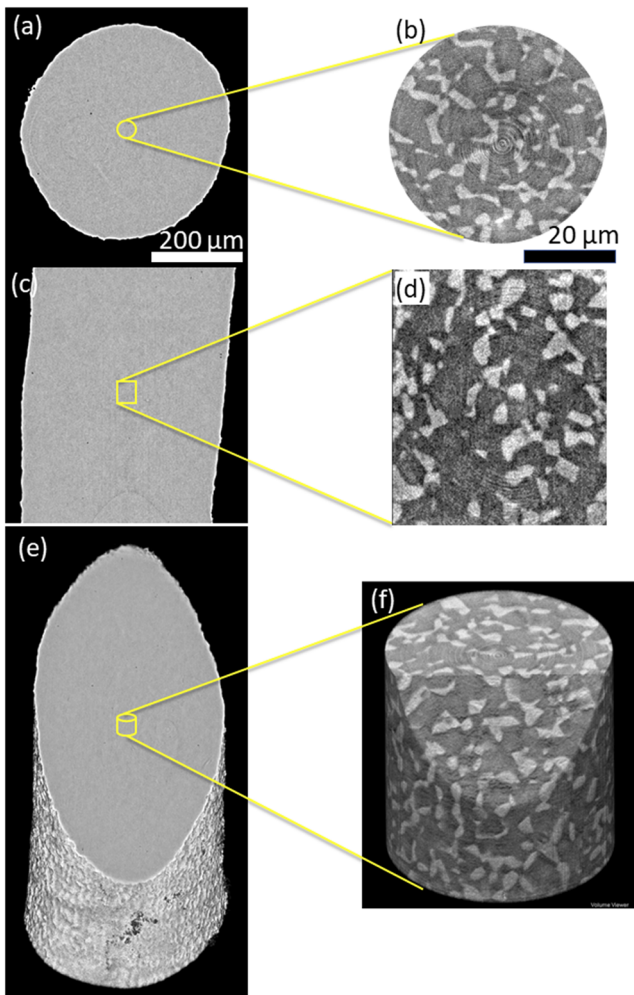
B. Fine structures of mouse bone

Low radiation damage is one of the motivating factors for using high-energy x rays. It enables detailed observations of medical and biological samples. Bones contain abundant cells called osteocytes,
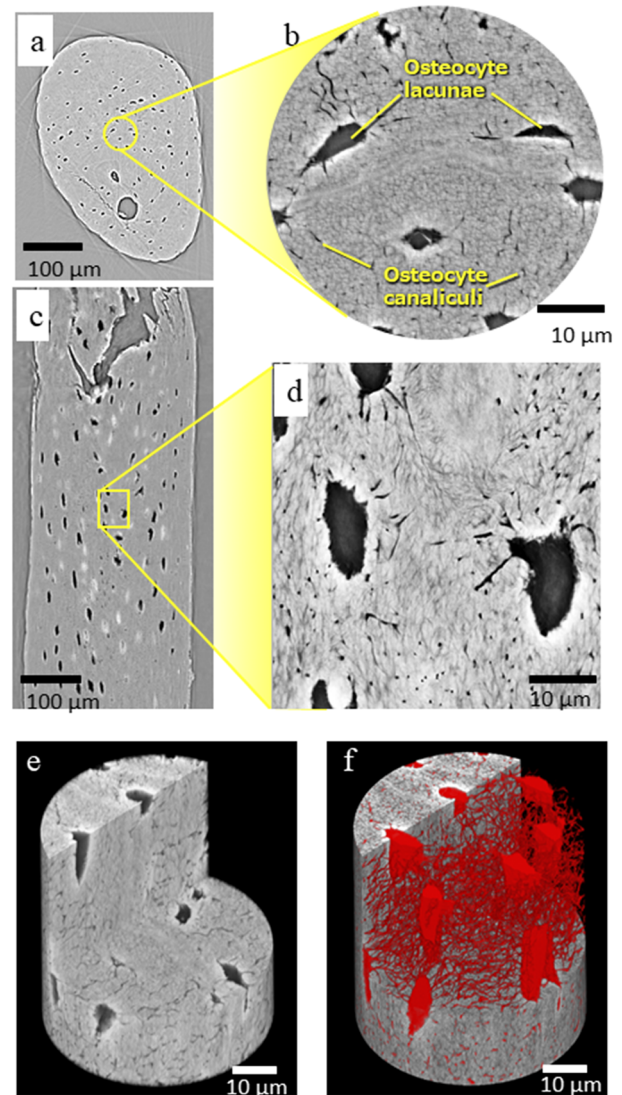

FIG. 12. Carbon steel Fe–0.1C–5Mn–1Si imaged via multiscale CT. (a) Virtual cross section, (c) longitudinal section, and (e) volume-rendering representation measured in the micro-CT mode. (b), (d), and (f) depict high-magnification nano-CT images of the ROIs delineated in (a), (c), and (e), respectively. In the micro-CT mode, the x-ray energy was 37.7 keV, the pixel size was 0.52 μm, the exposure time was 60 ms, and 1800 images were acquired over a 180° rotation. The nano-CT mode had an x-ray energy of 30 keV, a Zernike-phase contrast mode was applied, and magnification was 220×. A 200-μm-thick GAGG:Ce single crystal (Hamamatsu Photonics, Japan) was used as the scintillator for the x-ray image detector. The effective pixel size was 61.8 nm, the exposure time was 2 s, and 1800 images were acquired over a 180° rotation.

FIG. 13. Mouse fibula imaged via multiscale CT showing the network of osteocyte lacunae and canaliculi. Virtual cross sections at (a) low and (b) high magnification, and longitudinal sections at (c) low and (d) high magnifications through the volume-rendering representation. A 3D image of the ROI (e) was superimposed on the pseudo-color image of the lacuno-canalicular system (red). (a) and (c) were obtained in the micro-CT mode, and (b) and (d)–(f) were obtained in the nano-CT mode. In the micro-CT mode, the x-ray energy was 20 keV, the pixel size was 0.52 μm, the exposure time was 50 ms, and 1800 images were acquired over a 180° rotation. The nano-CT mode had an x-ray energy of 20 keV, a Zernike-phase contrast mode was applied, and magnification was 330×. A 200-μm-thick LuAG:Ce single crystal (Hamamatsu Photonics, Japan) was used as the scintillator for the x-ray image detector. The effective pixel size was 25.7 nm, the exposure time was 1 s, and 1800 images were acquired over a 180° rotation.

the reasonably low degree of artifacts, image segmentation can be used to quantitatively analyze the amount and morphologies of the dispersed austenite phase. It can be observed from Fig. 12 that the retained austenite phase appears to be particulate in nature and is almost discontinuously dispersed. Additionally, some austenite particles are partly interconnected. Generally, the retained austenite phase gradually transforms into the harder martensite phase upon loading. The retained austenite phase gradually shrinks and disappears as loading continues, indicating that such time-evolutionary behavior can be clearly visualized using this imaging technique.

FIG. 14. Murchison meteorite imaged via multiscale CT. (a) Virtual cross section of the entire sample (a pixel size of 3 μm). (b) Interior image of the circled ROI in (a) measured in the micro-CT mode. (c) Interior image of the circled ROI in (b) measured in the nano-CT mode. In the micro-CT mode, the x-ray energy was 37.7 keV, the pixel size was 0.52 μm, the exposure time was 50 ms, and 1800 images were acquired over a 180° rotation. In the nano-CT mode, the x-ray energy was 37.7 keV, and magnification was 175×. A 200-μm-thick GAGG:Ce single crystal (Hamamatsu Photonics, Japan) was used as the scintillator for the x-ray image detector. The effective pixel size was 38.9 nm, the exposure time was 2 s, and 1800 images were acquired over a 180° rotation.
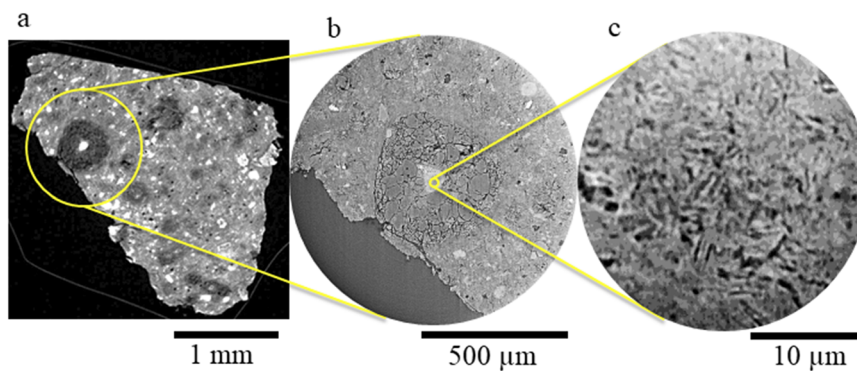
which are found in lacunae. The osteocyte lacuno-canalicular system, which is a large network, is critical for maintaining the bone matrix and has been analyzed via SR.[51] Figure 13 depicts an adult mouse fibula, which is smaller of the two long bones of the lower leg. CT imaging of the fibula at its smallest diameter (~300 μm) provided a full cross-sectional view [Fig. 13(a)]. Additionally, magnification of the circled ROI revealed osteocyte lacunae and canaliculi of ~0.3 μm diameter [Fig. 13(b)]. The long axes of the osteocyte lacunae were parallel to the long axis of the bone [Figs. 13(c) and 13(d)]. A 3D image of the magnified ROI [Fig. 13(e)] was superimposed on the pseudo-colored void that corresponded to the lacuno-canalicular system, revealing the extension of numerous canaliculi from individual osteocyte lacunae [Fig. 13(f)]. These data demonstrate that the new optics system enables analysis of the lacuna-canalicular system and other fine structures in biological samples at a high nano-CT resolution in a defined ROI, while providing a wide FOV in the micro-CT.

C. Extraterrestrial materials

A nondestructive multiscale CT measurement of a small particle of the Murchison meteorite, which is a type of carbonaceous chondrite, is depicted in Fig. 14. The CT image of the entire sample is depicted in Fig. 14(a). A spherical polycrystal object called a chondrule is observed in the circled region that might be comprised of porphyritic olivine-pyroxene (POP), which maintains original olivine and pyroxene without aqueous alteration. A bright region is observed at the center of the chondrule. Figure 14(b) depicts the interior CT image obtained in the micro-CT mode. Cracks are observed along the interface of the mineral grain boundary. Figure 14(c) depicts the interior CT image of the central region of the chondrule obtained in the nano-CT mode. A fibrous-like fine-grained crystalline structure (width: ~1 μm, length: several tens of micrometers), characteristic of a hydrous mineral, is observed. Because the conditions under which liquid water enters the anhydrous silicate POPs are severely limited, the evolution of these types of meteorites may be understood by carefully analyzing these conditions. The carbonaceous chondrite group may have originated

from C- and B-type asteroids, such as "RYUGU" and "BENNU," which are the destinations of the ongoing sample-return missions by Japan and the United States, respectively. The Murchison meteorite is considered as an analogous case for analyzing the samples to be returned by these space missions. Because the subdivision of the sample and exposure of the ROI to the terrestrial atmosphere may cause deterioration and/or destruction of minerals in the sample, the multiscale CT, which enables the nondestructive observation of the ROI, should prove effective in these observations. However, because it is difficult to determine the chemical states of these mineral phases via CT measurements alone, it will first be necessary to select and apply a suitable measurement method, for example, microbeam x-ray diffraction analysis, to examine these chemical states in the near future.

VI. CONCLUSION

In this paper, high-energy x-ray nano-CT, which is based on full-field x-ray microscopy and can be used in the energy region of 15 keV–37.7 keV, was described. An A-FZP developed for high-energy x-ray imaging was used as the objective lens. Furthermore, a 165-m-long optical tube enabled a magnification greater than 100× over the x-ray energy range used. Fine 3D structures with linewidths of 75 nm–100 nm were resolved via CT measurements to nearly diffraction-limited resolution within measurement times of 30 min–60 min. Multiscale CT imaging through the use of nano-CT and micro-CT allowed for the nondestructive nanoscale 3D observation of bulky samples (~1 mm), e.g., metals, biological specimens, and extraterrestrial materials.

DATA AVAILABILITY

The data that support the findings of this study are available from the corresponding author upon reasonable request.

REFERENCES

[1]V. De Andrade, A. Deriy, M. J. Wojcik, D. Gürsoy, D. Shu, K. Fezzaa, and F. De Carlo, SPIE Newsroom **10**, 006461 (2016).

[2]Y.-T. Chen, T.-N. Lo, Y. S. Chu, J. Yi, C.-J. Liu, J.-Y. Wang, C.-L. Wang, C.-W. Chiu, T.-E. Hua, Y. Hwu, Q. Shen, G.-C. Yin, K. S. Liang, H.-M. Lin, J. H. Je, and G. Margaritondo, Nanotechnology **19**, 395302 (2008).

[3]Y. Liu, J. C. Andrews, F. Meirer, A. Mehta, S. C. Gil, P. Sciau, Z. Mester, and P. Pianetta, AIP Conf. Proc. **1365**, 357 (2011).

[4]F. Meirer, S. Kalirai, J. N. Weker, Y. Liu, J. C. Andrews, and B. M. Weckhuysen, Chem. Commun. **51**, 8097 (2015).

[5]J. C. Andrews, P. Pianetta, F. Meirer, J. Chen, E. Almeida, M. C. H. van der Meulen, J. S. Alwood, C. Lee, J. Zhu, Y. Cui, R. Garrett, I. Gentle, K. Nugent, and S. Wilkins, AIP Conf. Proc. **1234**, 79 (2010).

[6]M.-T. Tang, Microscopy **64**, i37-2 (2015).

[7]Y.-F. Song and C.-C. Wang, Microscopy **64**, i37-1 (2015).

[8]E. M. Bolitho, C. Sanchez-Cano, H. Huang, I. Hands-Portman, M. Spink, P. D. Quinn, M. Harkiolaki, and P. J. Sadler, JBIC, J. Biol. Inorg. Chem. **25**, 295 (2020).

[9]C. Rau, A. J. Bodey, S. Marathe, S. Cipiccia, M.-C. Zdora, I. Zanette, U. H. Wagner, X. Shi, D. Batey, and M. Storm, in *Developments in X-Ray Tomography XI*, edited by B. Müller and G. Wang (SPIE, 2017), p. 28.

[10]Y. Suzuki, A. Takeuchi, Y. Terada, K. Uesugi, and R. Mizutani, AIP Conf. Proc. **1696**, 020013 (2016).

[11]M. Murugesan, A. Takeuchi, T. Fukushima, and M. Koyanagi, Jpn. J. Appl. Phys., Part 2 **58**, SBBC05 (2019).

[12]M. Feser, J. Gelb, H. Chang, H. Cui, F. Duewer, S. H. Lau, A. Tkachuk, and W. Yun, Meas. Sci. Technol. **19**, 094001 (2008).

[13]A. Aljdaimi, H. Devlin, M. Dickinson, T. Burnett, and T. J. A. Slater, Clin. Oral Inves. **23**, 2279 (2019).

[14]A. Momose and J. Fukuda, Med. Phys. **22**, 375 (1995).

[15]G. Requena, P. Cloetens, W. Altendorfer, C. Poletti, D. Tolnai, F. Warchomicka, and H. P. Degischer, Scr. Mater. **61**, 760 (2009).

[16]H. Fang, C. D. Versteylen, S. Zhang, Y. Yang, P. Cloetens, D. Ngan-Tillard, E. Brück, S. van der Zwaag, and N. H. van Dijk, Acta Mater. **121**, 352 (2016).

[17]F. Villar, L. Andre, R. Baker, S. Bohic, J. C. da Silva, C. Guilloud, O. Hignette, J. Meyer, A. Pacureanu, M. Perez, M. Salome, P. van der Linden, Y. Yang, and P. Cloetens, Synchrotron Radiat. News **31**, 9 (2018).

[18]I. Greving, M. Ogurreck, F. Marschall, A. Last, F. Wilde, T. Dose, H. Burmester, L. Lottermoser, M. Müller, C. David, and F. Beckmann, J. Phys.: Conf. Ser. **849**, 012056 (2017).

[19]M. Ogurreck, I. Greving, F. Marschall, H. Vogt, A. Last, J. J. Do Rosario, E. W. Leib, F. Beckmann, F. Wilde, and M. Müller, AIP Conf. Proc. **1696**, 020008 (2016).

[20]F. Marschall, A. Last, M. Simon, M. Kluge, V. Nazmov, H. Vogt, M. Ogurreck, I. Greving, and J. Mohr, J. Phys.: Conf. Ser. **499**, 012007 (2014).

[21]M. Stampanoni, F. Marone, J. Vila-Comamala, S. Gorelick, C. David, P. Trtik, K. Jefimovs, and R. Mokso, AIP Conf. Proc. **1365**, 239 (2010).

[22]A. Takeuchi, K. Uesugi, Y. Suzuki, S. Itabashi, and M. Oda, J. Synchrotron Radiat. **24**, 586 (2017).

[23]Y. Suzuki, K. Uesugi, N. Takimoto, T. Fukui, K. Aoyama, A. Takeuchi, H. Takano, N. Yagi, T. Mochizuki, S. Goto, K. Takeshita, S. Takahashi, H. Ohashi, Y. Furukawa, T. Ohata, T. Matsushita, Y. Ishizawa, H. Yamazaki, M. Yabashi, T. Tanaka, H. Kitamura, and T. Ishikawa, AIP Conf. Proc. **705**, 344 (2004).

[24]D. Weiß, G. Schneider, B. Niemann, P. Guttmann, D. Rudolph, and G. Schmahl, Ultramicroscopy **84**, 185 (2000).

[25]A. Takeuchi, K. Uesugi, H. Takano, and Y. Suzuki, Rev. Sci. Instrum. **73**, 4246 (2002).

[26]A. Takeuchi, K. Uesugi, Y. Suzuki, and S. Aoki, Jpn. J. Appl. Phys., Part 1 **40**, 1499 (2001).

[27]Y. Suzuki, H. Toda, and C. Schroer, *Advanced Tomographic Methods in Materials Research and Engineering*, edited by J. Banhart (Oxoford University Press, 2008).

[28]A. Takeuchi and Y. Suzuki, Microscopy **69**, 259–279 (2020).

[29]I. Snigireva, A. Snigirev, V. Kohn, V. Yunkin, M. Grigoriev, S. Kuznetsov, G. Vaughan, and M. Di Michiel, Phys. Status Solidi A **204**, 2817 (2007).

[30]S. Werner, S. Rehbein, P. Guttman, S. Heim, and G. Schneider, J. Phys.: Conf. Ser. **186**, 012079 (2009).

[31]W. Chao, J. Kim, S. Rekawa, P. Fischer, and E. H. Anderson, Opt. Express **17**, 17669 (2009).

[32]J. Vila-Comamala, K. Jefimovs, T. Pilvi, M. Ritala, S. S. Sarkar, H. H. Solak, V. A. Guzenko, M. Stampanoni, F. Marone, J. Raabe, G. Tzvetkov, R. H. Fink, D. Grolimund, C. N. Borca, B. Kaulich, and C. David, J. Phys.: Conf. Ser. **186**, 012078 (2009).

[33]J. Vila-comamala, S. Gorelick, E. Färm, C. M. Kewish, A. Diaz, R. Barrett, V. A. Guzenko, M. Ritala, and C. David, Opt. Express **19**, 175 (2011).

[34]I. Mohacsi, I. Vartiainen, M. Guizar-Sicairos, P. Karvinen, V. A. Guzenko, E. Müller, E. Färm, M. Ritala, C. M. Kewish, A. Somogyi, and C. David, Opt. Express **23**, 776 (2015).

[35]H. Takano, T. Tsuji, T. Hashimoto, T. Koyama, Y. Tsusaka, and Y. Kagoshima, Appl. Phys. Express **3**, 076702 (2010).

[36]C. Chang and A. Sakdinawat, Nat. Commun. **5**, 4243 (2014).

[37]D. Rudolph, B. Niemann, and G. Schmahl, Proc. SPIE **0316**, 103 (1981).

[38]N. Kamijo, S. Tamura, Y. Suzuki, and H. Kihara, Rev. Sci. Instrum. **66**, 2132 (1995).

[39]T. Koyama, H. Takano, S. Konishi, T. Tsuji, H. Takenaka, S. Ichimaru, T. Ohchi, and Y. Kagoshima, Rev. Sci. Instrum. **83**, 013705 (2012).

[40]Y. Suzuki, A. Takeuchi, K. Uesugi, M. Awaji, M. Yasumoto, S. Tamura, and N. Kamijo, IPAP Conf. Ser. **7**, 47–49 (2006).

[41]A. Takeuchi, K. Uesugi, and Y. Suzuki, J. Phys.: Conf. Ser. **849**, 012055 (2017).

[42]M. Oda, A. Ozawa, and Y. Hideo, J. Vac. Sci. Technol., B: Microelectron. Nanometer Struct. **11**, 37 (1993).

[43]A. Ozawa, T. Tamamura, T. Ishii, H. Yoshihara, and T. Kagoshima, Microelectron. Eng. **35**, 525 (1997).

[44]M. Sekimoto, A. Ozawa, T. Ohkubo, H. Yoshihira, M. Kakuchi, and T. Tamura, in *X-Ray Microscopy II*, edited by D. Sayre, M. Howells, J. Kirz, and H. Rarback (Springer-Verlag, Berlin, 1988), p. 178.

[45]A. G. Michette, *Optical Systems for Soft X Rays* (Springer US, 1986), pp. 165–215.

[46]J. Kirz, J. Opt. Soc. Am. **64**, 301 (1974).

[47]A. Takeuchi, K. Uesugi, and Y. Suzuki, J. Phys.: Conf. Ser. **186**, 012020 (2009).

[48]Y. Suzuki, A. Takeuchi, K. Uesugi, and M. Hoshino, AIP Conf. Proc. **1365**, 160 (2010).

[49]S. Tamura, M. Yasumoto, N. Kamijo, Y. Suzuki, M. Awaji, A. Takeuchi, H. Takano, and K. Handa, J. Synchrotron Radiat. **9**, 154 (2002).

[50]A. Takeuchi, K. Uesugi, M. Uesugi, F. Yoshinaka, and Nakamura, Microsc. Microanal. **24**, 108 (2018).

[51]N. Nango, S. Kubota, T. Hasegawa, W. Yashiro, A. Momose, and K. Matsuo, Bone **84**, 279 (2016).